

Supplementary information

The formation, reactivity and transformation pathways of formaldehyde in the methanol-to- hydrocarbons conversion

*Vladimir Paunović,^{*a} Xiangkun Wu,^b Luca Maggiulli,^{ab} Davide Ferri,^b Patrick Hemberger,^b*

*Andras Bodi^b and Jeroen A. van Bokhoven^{*ab}*

^a Institute for Chemical and Bioengineering, ETH Zurich, Vladimir-Prelog-Weg 1, 8093
Zurich, Switzerland

^b Paul Scherrer Institute, Forschungsstrasse 111, 5232 Villigen, Switzerland

S1. Supplementary experimental information

S1.1. Catalyst characterization. Micropore volumes and surface areas of the zeolites were calculated from the nitrogen isotherms recorded at 77 K using a Micromeritics 3D Flex automatic surface area and pore-size analyzer after degassing the samples (*ca.* 60 mg) at 573 K and 10 mbar for 12 h. Powder X-ray diffraction (PXRD) patterns were collected at Bragg-Brentano geometry using a PANalytical X'Pert PRO-MPD diffractometer with Cu K_{α} radiation ($\lambda = 1.54 \text{ \AA}$) generated by a 2.2 kW Cu anode, which was operated at $U = 40 \text{ kV}$ and $I = 20 \text{ mA}$. The data were recorded in the 2θ range of 10° – 50° using a step size of 0.014° and an acquisition time of 1.6 s per step. The silicon, aluminum, and calcium contents of the zeolite catalysts were analyzed by scanning electron microscopy (SEM, JSM-7100F) using a Si(Li) 30 mm^2 Ametek-EDAX EDX detector operated at 15.0 keV at a working distance of 10.0 mm. Solid-state ^{27}Al magic-angle spinning nuclear magnetic resonance (^{27}Al MAS NMR) spectroscopy measurements were performed on a Bruker Avance 400 spectrometer equipped with a 4 mm probe head. The samples were hydrated over an aqueous NH_4NO_3 solution (1 M) for 48 h and then filled into 4 mm zirconia rotors. The spectra were recorded at a resonance frequency of 104.3 MHz using a single-pulse excitation with a recycle delay of 1 s, a sweep width of 400 ppm, and 4500 (Z₁₅ and sZ₁₅) or 13000 (Z₄₀, sZ₄₀, and CaZ₄₀) accumulations. The magnetic field and the ppm axis were calibrated using the ^{13}C MAS NMR spectrum of adamantane (at 38.52 ppm) as an external secondary standard. The spectra were normalized to the sample weight. Fourier transform infrared spectroscopy (FTIR) measurements of the adsorbed pyridine were performed on an Excalibur spectrometer equipped with a DTGS detector. Self-supported discs (disc weight *ca.* 17 mg, disc area *ca.* 1.5 cm^2) of zeolites were placed in a quartz FTIR cell and degassed at 723 K and vacuum better than 5×10^{-6} bar for 3 h. Background FTIR spectra were collected after cooling to room temperature. Pyridine vapors (2.5×10^{-4} bar) were then dosed. The amount of adsorbed pyridine was analyzed by recording

the spectra after evacuating the sample at 423 K (all acid sites) and then at 573 K (strong acid sites) under a vacuum better than 5×10^{-6} bar for 1 h. The FTIR spectra were acquired by accumulating 128 scans in the range 650-4000 cm^{-1} with a nominal resolution of 4 cm^{-1} . The concentration of BAS and LAS was determined by integrating the FTIR bands at 1546 cm^{-1} and 1456 cm^{-1} , respectively, and by using the previously reported molar integral excitation coefficients of $\epsilon_{\text{LAS}} = 0.96 \text{ cm } \mu\text{mol}^{-1}$ and $\epsilon_{\text{BAS}} = 0.73 \text{ cm } \mu\text{mol}^{-1}$.¹ The calculated values of BAS and LAS are reported in **Table S1**.

S1.2. Catalyst testing in methanol-to-hydrocarbons conversion. Methanol-to-hydrocarbons (MTH) conversion was also performed in a home-made continuous flow microreactor set-up hosting a quartz reactor (internal diameter, $d_i = 6$ mm) loaded with a fixed catalyst bed. The catalysts ($W_Z = 0.015\text{-}0.150$ g, $d_p = 0.18\text{-}0.25$ mm) were well mixed with quartz particles (Thommen-Furler, washed in HNO_3 and calcined, $W_Q:W_Z = 6\text{-}30$, $d_p = 0.355\text{-}0.420$ mm) and loaded between two plugs of quartz wool. The reactor was placed into a tubular electric oven and the reaction temperature was regulated by a Type K thermocouple, the tip of which was positioned in the center of the catalyst bed. Methanol (CH_3OH , Sigma-Aldrich, $\geq 99.9\%$) was supplied by a syringe pump (Chemyx Fusion 6000) to a vaporizer operated at 413 K, where it was mixed with argon (Ar, PanGas, 5.0) fed by a digital mass flow controller (MFC). In the co-feeding experiments: 1-methyl-1-cyclohexene (Acros $>98\%$), *cis*-hex-3-en-1-ol (precursor of hexadiene, Acros, 98%), toluene (Sigma-Aldrich, $>99.5\%$), 2,4-hexadien-1-ol (precursor of hexatriene, abcr, 98%), cyclopent-3-enol (precursor of cyclopentadiene, Fluorochem, 97%), styrene (Sigma-Aldrich, $\geq 99.5\%$), indene (Sigma-Aldrich, $\geq 98\%$), and formaldehyde (Fisher, 37 wt% in water) were added to methanol in appropriate amounts and supplied by a syringe pump. The reaction pressure was monitored by a digital pressure indicator (Keller) positioned above the reactor. Prior to reaction, the catalyst bed was heated up to 823 K under argon flow ($F_{\text{Ar}} = 300 \text{ cm}^3_{\text{STP}} \text{ min}^{-1}$) at a heating rate of 10 K min^{-1} , then calcined under flowing oxygen

(O₂, PanGas, 5.0, $F_{O_2} = 100 \text{ cm}^3_{\text{STP}} \text{ min}^{-1}$) for 0.5 h to remove potential impurities from the zeolite. The flow was then switched to argon, and the reactor was cooled to the reaction temperature, wherein it was stabilized for *ca.* 1 h. The reaction mixture, pre-stabilized through a bypass line, was then admitted to the reactor. The MTH reaction was carried out at $T = 673 \text{ K}$ or 773 K and $P = 1.6 \text{ bar}$ by feeding $F_{\text{CH}_3\text{OH}} = 0.08 \text{ cm}^3_{\text{liq}} \text{ min}^{-1}$ ($45 \text{ cm}^3_{\text{STP}} \text{ min}^{-1}$) of methanol diluted with $F_{\text{Ar}} = 190 \text{ cm}^3_{\text{STP}} \text{ min}^{-1}$ of argon unless otherwise stated. This corresponds to a methanol concentration of $c_{\text{CH}_3\text{OH}} = 19.1 \text{ mol}\%$ and $WHSV = 25\text{-}253 \text{ g}_{\text{CH}_3\text{OH}} \text{ g}_Z^{-1} \text{ h}^{-1}$. The methanol, dimethyl ether, and hydrocarbon contents of the reactor outlet feed were analyzed online by a gas chromatograph equipped with a flame ionization detector (GC-FID) and HP PLOT-Q column. The conversion X , the selectivity to hydrocarbon products C_xH_y ($S_{\text{C}_x\text{H}_y}$), the cumulative turnover capacity CT , hydrogen-transfer index HTI , and the descriptor for the propagation of the arene over alkene MTH cycle $D_{\text{E}/2\text{MBt}}$,² and cumulative values of the product distribution parameters, *i.e.*, $CS_{\text{C}_x\text{H}_y}$, $CHTI$, $CD_{\text{E}/2\text{MBt}}$ were calculated according to **Eqs. S3-8**, in which $\dot{n}_{\text{C}_x\text{H}_y\text{O}_z, \text{in}}$ and $\dot{n}_{\text{C}_x\text{H}_y\text{O}_z, \text{out}}$ denote the inlet and outlet molar flows of $\text{C}_x\text{H}_y\text{O}_z$. The time integrals were approximated by trapezoidal rule. The carbon balance was higher than 96% in all experiments.

$$X = \frac{\dot{n}_{\text{CH}_3\text{OH}, \text{in}} - (\dot{n}_{\text{CH}_3\text{OH}, \text{out}} + 2 \times \dot{n}_{\text{DME}, \text{out}})}{\dot{n}_{\text{CH}_3\text{OH}, \text{in}}}, \% \quad \text{S1}$$

$$S_{\text{C}_x\text{H}_y} = \frac{x\dot{n}_{\text{C}_x\text{H}_y}}{\sum_1^n x\dot{n}_{\text{C}_x\text{H}_y}} \times 100, \% \quad \text{S2}$$

$$CT = WHSV \int_0^t X dt, \text{ g}_{\text{CH}_3\text{OH}} \text{ g}_{\text{CH}_3\text{OH}}^{-1} \quad \text{S3}$$

$$HTI = \frac{\sum_{x=2}^4 x \dot{n}_{C_x H_{2x+2}}}{\sum_{x=2}^4 x \dot{n}_{C_x H_{2x+2}} + \sum_{x=2}^4 x \dot{n}_{C_x H_{2x}}}, \quad - \quad S4$$

$$D_{C_2H_4/mC_5H_{10,12}} = \frac{2 \dot{n}_{C_2H_4}}{5(\dot{n}_{C_5H_{10,2-methybutene}} + \dot{n}_{C_5H_{12,2-methybutane}})}, \quad - \quad S5$$

$$CS_{C_x H_y} = \frac{\int x \dot{n}_{C_x H_y} dt}{\int \sum_1^n x \dot{n}_{C_x H_y} dt} \times 100, \quad \% \quad S6$$

$$CHTI = \frac{\int \sum_{x=2}^4 x \dot{n}_{C_x H_{2x+2}} dt}{\int \left(\sum_{x=2}^4 x \dot{n}_{C_x H_{2x+2}} + \sum_{x=2}^4 x \dot{n}_{C_x H_{2x}} \right) dt}, \quad - \quad S7$$

$$CD_{C_2H_4/mC_5H_{10,12}} = \frac{2 \int \dot{n}_{C_2H_4} dt}{5 \int (\dot{n}_{C_5H_{10,2-methybutene}} + \dot{n}_{C_5H_{12,2-methybutane}}) dt}, \quad - \quad S8$$

S1.3. Analysis of reactants and products by operando PEPICO spectroscopy. The signals of specific MTH species were acquired at specific mass-to-charge ratios (m/z) and photon energies ($h\nu$), which are higher than the neutral ionization energy of the targeted molecules and lower than the dissociative photoionization thresholds of other MTH species that could yield the fragment ions of the same m/z species (*e.g.*, $CH_3OH + h\nu \rightarrow CH_2O^+ + 2 H + e^-$) (Table S2). Fragmentation is thus quantitatively suppressed, which ensures that the detected ions exclusively represent the parent molecules that have the same m/z ratio. The MTH reactants, specific products, and intermediates are isomer-selectively assigned by comparison with either reference photoionization spectra, threshold photoionization spectra, or Franck-

Condon simulations. The contributions of the ‘wall-catalyzed’ methanol dehydrogenation to formaldehyde formation were minimized by using a quartz tubular reactor and a highly pure quartz diluent. Therein, the productivity of formaldehyde over zeolite catalysts was calculated by subtracting a small ‘background’ productivity of this intermediate in a zeolite-free reactor from measured yield.

Reactant conversion X and product yields Y were calculated according to **Eqs S9,10**, respectively, in which $S_{\text{CH}_3\text{OH}, \text{out}}(h\nu)$, $S_{\text{DME}, \text{out}}(h\nu)$, $S_{\text{C}_x\text{H}_y\text{O}_z, \text{out}}(h\nu)$, and $S_{\text{Xe}, \text{out}}(h\nu)$ represent the integrated ion counts of methanol, DME, the products $\text{C}_x\text{H}_y\text{O}_z$, and xenon at photon energy $h\nu$. $C_{\text{DME}/\text{CH}_3\text{OH}}$ is the calibrated DME over methanol conversion factor, $\sigma_{\text{CH}_3\text{OH}}(h\nu)$ and $\sigma_{\text{C}_x\text{H}_y\text{O}_z}(h\nu)$ represent the photoionization cross sections of methanol and the product $\text{C}_x\text{H}_y\text{O}_z$ at the photoionization energy $h\nu$ (**Table S2**). $D_{\text{CH}_3\text{OH}}(h\nu)$ and $D_{\text{C}_x\text{H}_y\text{O}_z}(h\nu)$ are the mass discrimination factors of methanol and product $\text{C}_x\text{H}_y\text{O}_z$, which are close to unity as recently determined using the same endstation and techniques.³ The subscripts “in” and “out” in the designations of the integrated ion areas indicate the values recorded in actual versus blank experiments performed in an empty quartz reactor at temperature of 473 K, respectively. Because the $\sigma_{\text{C}_x\text{H}_y\text{O}_z}(h\nu)$ factors are typically determined with a relative error of *ca.* 15%, the absolute values of the estimated product yields in the *i*²PEPICO experiments can deviate *ca.* $\pm 15\%$ from their true values. Nonetheless, because this error affects the product distribution over all catalysts equally, it does not affect the measured relative differences in product yields among the different catalyst samples.

In ¹³C methanol-labeling experiments, the fraction of the ¹³C carbon $f_{13\text{C}, \text{C}_x\text{H}_y\text{O}_z}$ incorporated in the corresponding compound $\text{C}_x\text{H}_y\text{O}_z$ was calculated according to **Eq. S11**, in which S_i is the integrated ion counts of the isotopomer with i number of incorporated ¹³C atoms.

Franck–Condon simulations were performed using density functional theory at the B3LYP/6–311++G(d,p) level at a temperature of 500 K. The stick spectra were convoluted with a Gaussian of 150 cm^{-1} full width at half maximum (*FWHM*) to account for the rotational envelope. The ionization energies were calculated using the G4 composite method.

$$X = \frac{\frac{S_{\text{CH}_3\text{OH}, \text{in}}(E)}{S_{\text{Xe}, \text{in}}(E)} - \frac{S_{\text{CH}_3\text{OH}, \text{out}}(h\nu) + C_{\text{DME/CH}_3\text{OH}} S_{\text{DME}, \text{out}}(h\nu)}{S_{\text{Xe}, \text{out}}(h\nu)}}{\frac{S_{\text{CH}_3\text{OH}, \text{in}}(h\nu)}{S_{\text{Xe}, \text{in}}(h\nu)}} \times 100, \% \quad \text{S9}$$

$$Y_{\text{C}_x\text{H}_y\text{O}_z} = \frac{\frac{S_{\text{C}_x\text{H}_y\text{O}_z, \text{out}}(h\nu)}{S_{\text{Xe}, \text{out}}(h\nu)} \times \frac{\sigma_{\text{CH}_3\text{OH}}(h\nu)}{\sigma_{\text{C}_x\text{H}_y\text{O}_z}(h\nu)} \times \frac{D_{\text{CH}_3\text{OH}}(h\nu)}{D_{\text{C}_x\text{H}_y\text{O}_z}(h\nu)} \times x}{\frac{S_{\text{CH}_3\text{OH}, \text{in}}(h\nu)}{S_{\text{Xe}, \text{in}}(h\nu)}} \times 100, \% \quad \text{S10}$$

$$f_{^{13}\text{C}, \text{C}_x\text{H}_y\text{O}_z} = \frac{\sum_{i=0}^{i=x} S_i}{x \sum_{i=0}^{i=x} S_i} \times 100, \% \quad \text{S11}$$

S1.4. Analysis of DR/UV-Vis spectra. *Operando* diffuse-reflectance UV-visible (DR/UV-Vis) spectroscopy analysis of the reaction intermediates confined in the pores of the zeolite was performed in a home-built plug-flow cell (rectangular cross section: 5×3 mm, length: 10 mm) closed with a calcium fluoride window. The preparation of the MTH reaction mixture and the analysis of the reaction products were performed by connecting the inlet and the outlet of the cell to the reactant feeding system and GC-FID analyzer, as detailed for the MTH reaction tests in the continuous-flow fixed-bed microreactor setup (Supplementary

Experimental Information S1.2). The catalysts ($W_Z = 0.023$ g, $d_p = 0.18$ - 0.25 mm) were loaded inside the cell and gently pressed against the calcium fluoride window. The catalyst bed was heated up to 723 K under argon flow ($F_{Ar} = 100$ cm³_{STP} min⁻¹) at a heating rate of 5 K min⁻¹ and then exposed to the flow of oxygen (O₂, PanGas, 5.0, $F_{O_2} = 50$ cm³_{STP} min⁻¹) for 0.5 h to remove potential impurities from the zeolite. The oxygen flow was then replaced with argon and the reactor was cooled to the reaction temperature and allowed to stabilize for *ca.* 1 h. Background reference spectra were collected before the reaction mixture was introduced. Thereafter, spectra were collected continuously at a frequency of 1 scan/s in absorbance mode, wherein the absorbance at pixel n is calculated using the measured signal intensities for current sample (I_{sample}), reference ($I_{\text{reference}}$), and dark (I_{dark}) data sets (**Eq. 12**). To determine the relative fraction of different spectral components, the acquired UV-Vis spectra were deconvoluted into 11 Gaussian peaks corresponding to the typical absorption regions of the representative zeolite-confined species (**Table S3**). The peak centers and their full widths at half maximum were kept constant. The relative fraction of each spectral component was calculated using **Eq. S13**, where S_i is the surface area of spectral component i .

$$\text{Absorbance} = -\log\left(\frac{I_{\text{sample}} - I_{\text{dark}}}{I_{\text{reference}} - I_{\text{dark}}}\right), - \quad \text{S12}$$

$$f_i = \frac{S_i}{\sum S_i}, - \quad \text{S13}$$

S2. Supplementary discussion

S2.1. Apparent reaction order of the formaldehyde formation. The observations (1) that formaldehyde formation in the low conversion regime of the MTH conversion is accompanied with the evolution of approximately equimolar amounts methane, and (2) that higher alkanes and aromatics are below the detection level (**Fig. 1** of the main Manuscript) suggest that hydrogen transfer between two methanol molecules is the primary source of formaldehyde formation. Previous work indicated that the latter reaction starts with dehydrogenation of methanol over BAS (Z-H), which leads to the formation of surface bound methyl species ($\text{CH}_3\text{-Z}$, **Eq. S14**).⁴ This step readily occurs at typical temperatures of the MTH reaction and can be considered as pseudo-equilibrated. In the second step, surface-bound methyl group reacts with methanol, which is probably loosely interacting with the neighboring oxygen atom of the BAS site. In the first approximation, this step involves a hydride transfer from “gas-phase” methanol molecule to surface-bound methyl group containing electrophilic carbon methanol *via* an Eley-Rideal-type mechanism (**Eq. S15**). The second step thus leads to the formation of methane, which is desorbed to the gas-phase, and surface bound hydroxymethyl group, *i.e.*, formaldehyde adsorbed on BAS ($\text{HOCH}_2\text{-Z}$), which can be desorbed in the third step (**Eq. S16**).



The second step (**Eq. S15**), is likely to be the rate-limiting (**Eq. S17**).⁴ Assuming that the first step (**Eq. S14**) is in the pseudo-equilibrium state (**Eq. S18**), the coverage of surface-bound methyl species can be determined by rearranging the **Eq. S18** into **Eq. S19**. The site-balance

equation assumes that BAS are primarily covered by methoxy-species, whereas in the first approximation, the adsorption of formaldehyde and water can be neglected (**Eq. S20**). The latter assumptions are based on significantly lower concentrations of formaldehyde and water with respect to methanol in the low conversion regime, and previously reported propensity of methanol to rapidly displace adsorbed water, and low potential of water to displace adsorbed methanol.⁵ Incorporation of **Eq. S19** into **Eq. S20** yields **Eq. S21**, which after simple rearrangements (**Eqs S22**) gives **Eq. S23**. In view of the previous assumptions, it can be further proposed that the term comprising equilibrium constant of methanol adsorption and methanol-to-water concentration ratio is significantly greater than one. This approximation anticipates that BAS are almost exclusively occupied by surface-bound methyl groups. Under these assumptions, the reaction rate of formaldehyde formation over BAS approximately follows the first order dependence with respect to methanol, as observed in the PEPICO experiments (**Eq. S24, Fig. 3** of the main manuscript). In overall, this expression indicates that since surface methyl species cover almost all the BAS sites, the productivity of formaldehyde will be primarily determined by the concentration of weakly interacting (gaseous) methanol species.

$$r = k_2 \theta_{Z-CH_3} c(\text{CH}_3\text{OH}_{(g)}) \quad \text{S17}$$

$$K_1 = \frac{\theta_{Z-CH_3} c(\text{H}_2\text{O}_{(g)})}{\theta_{Z-H} c(\text{CH}_3\text{OH}_{(g)})} \quad \text{S18}$$

$$\theta_{Z-CH_3} = K_1 \frac{\theta_{Z-H} c(\text{CH}_3\text{OH}_{(g)})}{c(\text{H}_2\text{O}_{(g)})} \quad \text{S19}$$

$$\theta_{Z-CH_3} + \theta_{Z-H} = 1 \quad \text{S20}$$

$$K_1 \frac{\theta_{Z-H} c(\text{CH}_3\text{OH}_{(g)})}{c(\text{H}_2\text{O}_{(g)})} + \theta_{Z-H} = 1 \quad \text{S21}$$

$$\theta_{\text{Z-H}} = \frac{1}{1 + K_1 \frac{c(\text{CH}_3\text{OH}_{(\text{g})})}{c(\text{H}_2\text{O}_{(\text{g})})}} \quad \text{S22}$$

$$\theta_{\text{Z-CH}_3} = \frac{K_1 \frac{c(\text{CH}_3\text{OH}_{(\text{g})})}{c(\text{H}_2\text{O}_{(\text{g})})}}{1 + K_1 \frac{c(\text{CH}_3\text{OH}_{(\text{g})})}{c(\text{H}_2\text{O}_{(\text{g})})}} \approx 1 \quad \text{S23}$$

$$r \approx k_2 c(\text{CH}_3\text{OH}_{(\text{g})}) \quad \text{S24}$$

S3. Supplementary tables

Table S1. Textural and acid properties of fresh ZSM-5 catalysts.

| Catalyst | $S_{\text{meso}}^{[a]}$ / | $S_{\text{BET}}^{[b]}$ / | $V_{\text{micro}}^{[a]}$ / | $V_{\text{total}}^{[c]}$ / | $c_{\text{BAS}}^{[e]}$ / $\mu\text{mol g}^{-1[f]}$ | | $c_{\text{LAS}}^{[f]}$ / $\mu\text{mol g}^{-1}$ | |
|----------|----------------------------|----------------------------|-----------------------------|-----------------------------|--|--------|---|--------|
| | $\text{m}^2 \text{g}^{-1}$ | $\text{m}^2 \text{g}^{-1}$ | $\text{cm}^3 \text{g}^{-1}$ | $\text{cm}^3 \text{g}^{-1}$ | all | strong | all | strong |
| Z15 | 24 | 323 | 0.16 | 0.22 | 759 | 391 | 205 | 172 |
| Z40 | 55 | 362 | 0.16 | 0.22 | 289 | 217 | 68 | 69 |
| CaZ40 | 80 | 311 | 0.14 | 1.14 | 63 | 26 | 268 | 60 |
| sZ15 | 36 | 314 | 0.14 | 0.22 | 171 | 87 | 161 | 112 |
| sZ40 | 59 | 379 | 0.16 | 0.24 | 160 | 125 | 71 | 49 |

[a] *t*-plot and [b] BET analysis of N₂ sorption isotherms. [c] From N₂ adsorbed volume at $p/p^0 = 0.99$. [d] FTIR analysis of pyridine adsorption at 423 (all) and 573 K (strong).

Table S2. Parameters relevant to species detection using PEPICO spectroscopy.

| Compound | m/z | PI threshold / eV ⁶ | $\sigma(h\nu)$ / MB ^[a] |
|--------------------------------|-------|--------------------------------|------------------------------------|
| CH ₃ OH | 32 | 10.84 ± 0.01 | 2.1 ⁷ |
| CH ₂ O | 30 | 10.88 ± 0.01 | 9.2 ^{8,9} |
| CH ₄ | 16 | 12.61 ± 0.01 | 15.5 ¹⁰ |
| C ₂ H ₄ | 28 | 10.51 ± 0.01 | 6.8 ^{11,12} |
| C ₃ H ₆ | 42 | 9.73 ± 0.01 | 11.2 ¹³ |
| C ₄ H ₆ | 54 | 9.07 ± 0.01 | 12.3 ⁷ |
| C ₄ H ₈ | 56 | 9.10–9.55 ^[b] | 10.6 ^{[c]10,14} |
| C ₄ H ₁₀ | 58 | 10.53–10.68 ^[b] | 3.5 ^{[c]10,14,15} |
| C ₅ H ₈ | 68 | 8.6–8.86/9.46 ^[b] | 21.5 ^{[c]14} |
| C ₅ H ₁₀ | 70 | 8.69–9.52 ^[b] | 14.6 ^{[c]14} |
| C ₅ H ₁₂ | 72 | 10.28–10.32 ^[b] | 11.7 ^{[c]16} |
| 1MB | 92 | 8.83 ± 0.01 ^[b] | 38.7 ¹⁷ |
| 2MB | 106 | 8.44–8.56 ^[b] | 44.1 ^{[c]17} |
| 3MB | 120 | 8.27–8.42 ^[b] | 47.4 ¹⁷ |

[a] The values of the photoionization cross sections correspond to $h\nu = 10.9$ eV, except for methane where the value is given for $h\nu = 13.6$ eV. Relative errors amount to ± 15%. [b] Ranges cover different structural isomers.

[c] Calculated as an average value for several isomers.

Table S3. Peak components used for DR/UV-Vis spectra deconvolution and their assignment.

| Peak center / cm^{-1} | FWHM / cm^{-1} | Assignment ¹⁸⁻²⁰ |
|--------------------------------|-------------------------|---|
| 38500±700 | 3000±300 | Neutral benzene derivatives |
| 35500±700 | 4000±300 | Monoenyl (cyclic/acyclic) carbenium ions |
| 32500±400 | 3000±300 | Monoenyl (cyclic/acyclic) carbenium ions |
| 28500±400 | 3300±300 | Lower MBs carbenium ions (up to <i>ca.</i> 4MB) Dienyl (cyclic/acyclic) carbenium ions |
| 26000±300 | 2400±300 | Higher MBs/ alkyl benzene carbenium ions |
| 24000±300 | 1800±300 | MNs carbenium ions |
| 23000±300 | 3300±300 | Charged and neutral MNs |
| 20000±200 | 2500±300 | Lower PAH |
| 18000±200 | 2000±300 | Higher PAH |
| 16500±150 | 1500±300 | Higher PAH |

S3. Supplementary figures

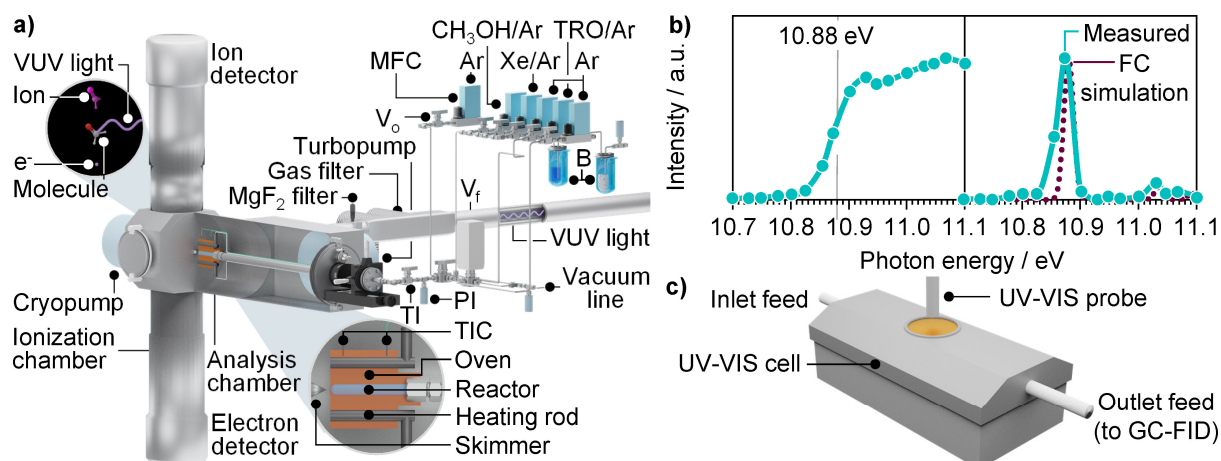


Fig. S1. a) Schematic representation of the PEPICO reactor setup and b) representative photoionization (left) and photoion threshold photoelectron (TPE) spectra (right) of *m/z* 30 species, demonstrating the detection of formaldehyde. Frank–Condon (FC) simulation of the TPE spectrum of formaldehyde is shown for comparison. c) Schematic representation of the plug-flow DR/UV-Vis cell.

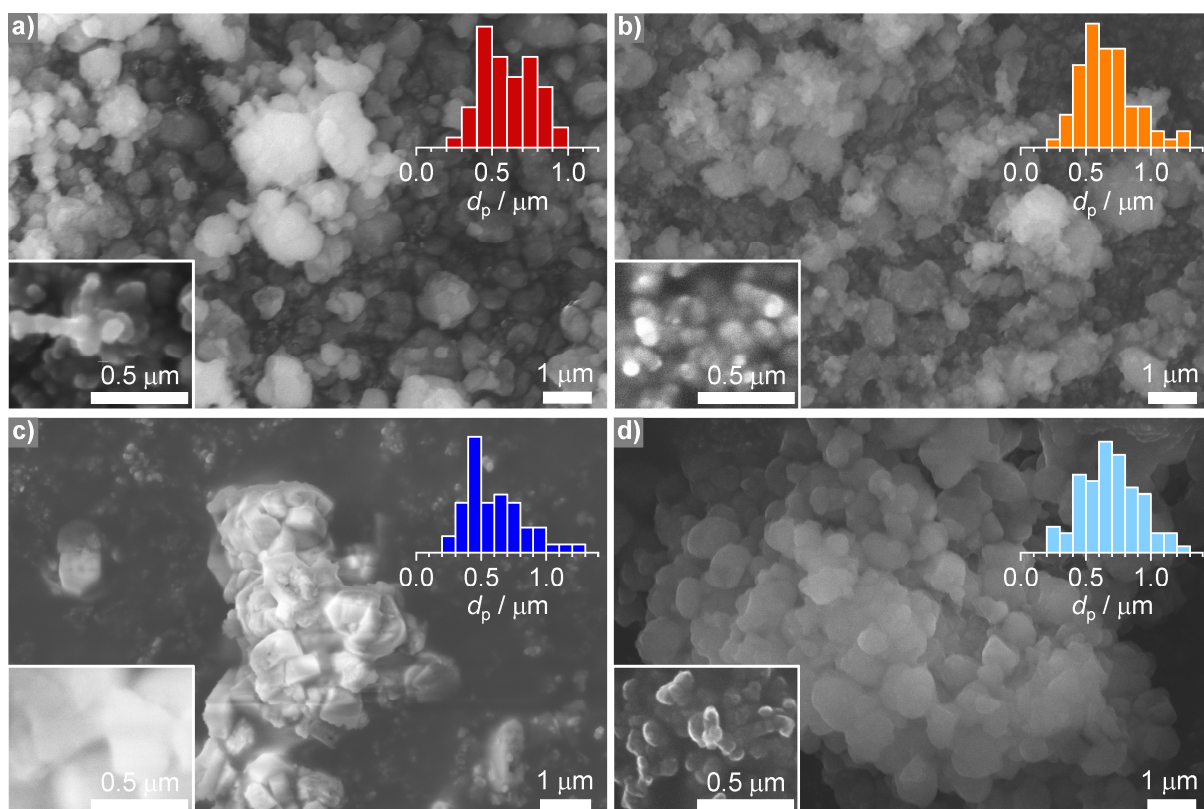


Fig. S2. Scanning electron micrographs (SEM) and the particle size distribution of fresh **a)** Z₁₅, **b)** Z₄₀, **c)** sZ₁₅, and **d)** sZ₄₀. The SEM analysis shows that the parent zeolites mostly contained crystals in the size range of *ca.* 0.4–1 μm . The inset SEM images indicate that particles comprise crystallites of *ca.* 60–80 nm crystallites, which is also supported by the PXRD analysis (*vide infra*, **Fig. S2**).

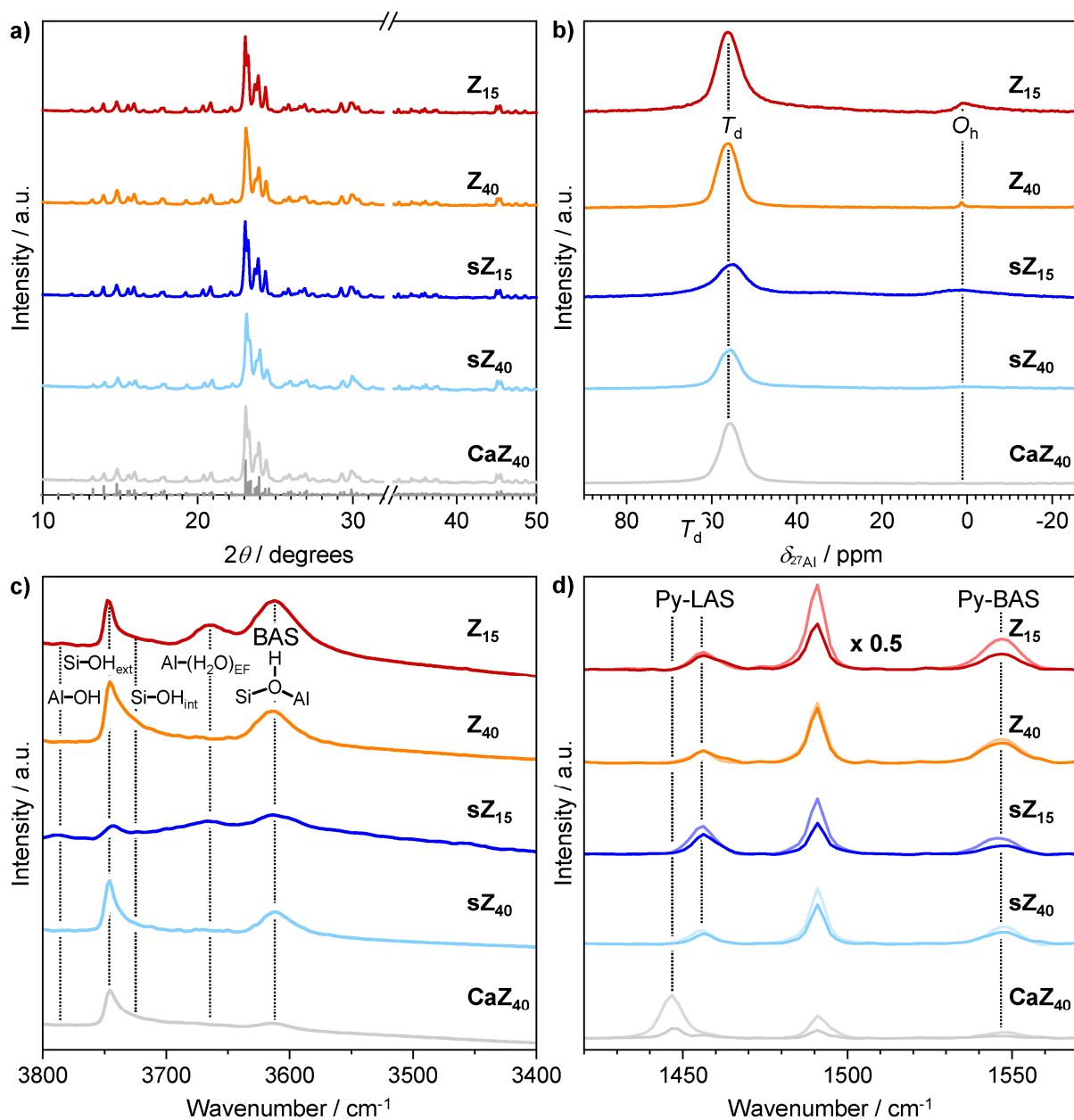


Fig. S3. a) Powder X-ray diffractograms, b) ^{27}Al magic angle spinning NMR spectra, and FTIR spectra of c) O-H stretching region, and d) adsorbed-pyridine FTIR spectra of the fresh Z₁₅, Z₄₀, sZ₁₅, sZ₄₀, and CaZ₄₀ zeolite catalysts. The measured diffractograms of all zeolites display the characteristic peaks of the reference ZSM-5 material, which are shown by the vertical lines below the measured signals. The analysis of the powder X-ray diffractograms indicates that the average crystallite size of *ca.* 60-80 nm, in agreement with the SEM analysis (*vide supra*). The ^{27}Al MAS NMR spectra display an intense resonance at *ca.* 56 ppm, which

can be ascribed to the tetrahedral (T_d), i.e., framework aluminum sites. Its intensity increases in the following order: $sZ_{40} \approx sZ_{15} < Z_{40} \approx CaZ_{40} < Z_{15}$, indicating that the fraction of framework aluminum sites increases in this order. In addition, the samples also display the resonance at *ca.* 0 ppm, which corresponds to octahedral (O_h) aluminum sites. The latter spectral feature is more pronounced in Z_{15} and sZ_{15} , indicating a high concentration of extra-framework aluminum site sites in these samples. The FTIR spectra of the O-H region indicate that intensity of the signal associated with BAS (*ca.* 3610 cm^{-1}) is following the order: $CaZ_{40} < sZ_{40} \approx sZ_{15} < Z_{40} < Z_{15}$. Moreover, the spectra of Z_{15} and sZ_{15} material display increased intensity of the bands associated with extra-framework or framework associated aluminum species: Al-(H₂O)_{EF} (3667 cm^{-1}) as well as Al-OH (3790 cm^{-1}) with respect to Z_{40} and sZ_{40} .²¹ In addition, the FTIR spectra indicate that the relative ratio between the signals associated with internal Si-OH_{int} (3725 cm^{-1}) and external Si-OH_{ext} (3745 cm^{-1}) silanols is particularly high for the sZ_{15} samples.^{22,23} Previous studies indicated that catalysts exhibiting a higher value of this ratio are more susceptible to coke-induced deactivation.^{22,23} The spectra acquired after pyridine adsorption exhibit the characteristic bands of the internal modes of pyridine interacting with Lewis acid sites (LAS, 1456 cm^{-1}) and BAS (1490 cm^{-1} , 1546 cm^{-1}).²⁴ The integrals of the 1546 cm^{-1} and 1456 cm^{-1} bands were used to quantify the BAS and LAS, the concentrations of which are reported in Supplementary Table S1. The relative intensities of the BAS band indicate an increase in the concentration of these sites in the following order: $CaZ_{40} < sZ_{40} \approx sZ_{15} < Z_{40} < Z_{15}$. Consistent with ²⁷Al MAS NMR and FTIR spectra recorded in the O-H stretching region, the FTIR spectra of the adsorbed pyridine indicate that Lewis acidity increases in the order: $Z_{40} \approx sZ_{40} < sZ_{15} < Z_{15} < CaZ_{40}$.

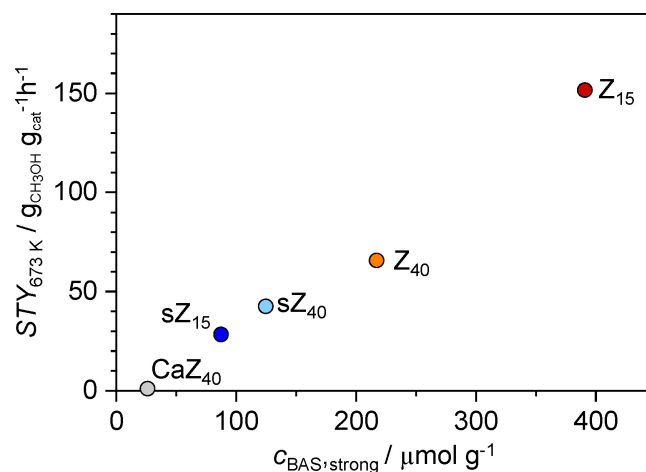


Fig. S4. The initial space-time yield, STY , in the MTH reaction at 673 K versus strong BAS concentration for different ZSM-5 zeolites used in this study. The initial STY measured in the incomplete conversion range of 25–85% displays a linear dependence on the concentration of BAS, in agreement with the central catalytic role of these sites in catalyzing the MTH conversion. Reaction conditions: $CH_3OH:Ar = 19:81$ mol%, $WHSV = 25$ – 253 $g_{CH_3OH} g_{cat}^{-1} h^{-1}$, $T = 673$, and $P = 1.6$ bar.

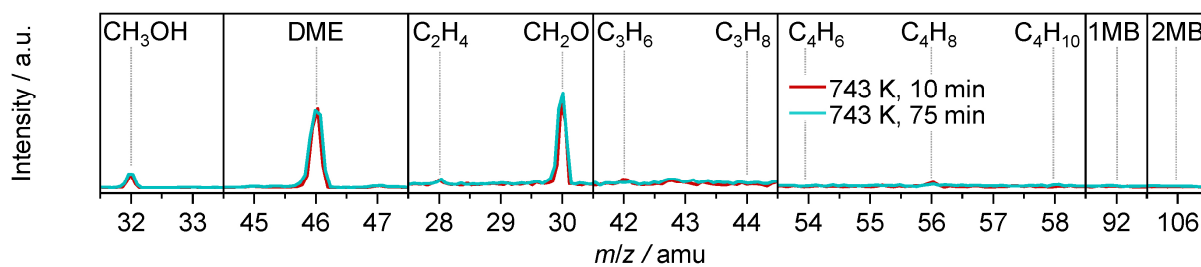


Fig. S5. Mass spectra of reactive species detected in the MTH conversion over CaZ_{40} catalysts at 743 K after 10 and 75 min of reaction. The spectra were recorded at $h\nu = 10.9$ eV. $\text{CH}_3\text{OH}:\text{Xe}:\text{Ar} = 1.95:0.15:97$ mol%, $WHSV = 1.4 \text{ g}_{\text{CH}_3\text{OH}} \text{ g}_{\text{cat}}^{-1} \text{ h}^{-1}$, $T = 621\text{--}743$ K, and $P = 0.4$ bar. The spectra recorded at after 75 min correspond to those acquired after 10 min of reaction, which shows that activity and product distribution of CaZ_{40} remained unaltered over long reaction time. This corroborates the assumption that that the concentration of HP species does not change significantly, as if it would otherwise lead to an increase of yield of C_{2+} hydrocarbon products. This result thus supports the hypothesis that the consumption of formaldehyde via the formation of dienes, arenes or HP species is greatly suppressed in this reaction regime.

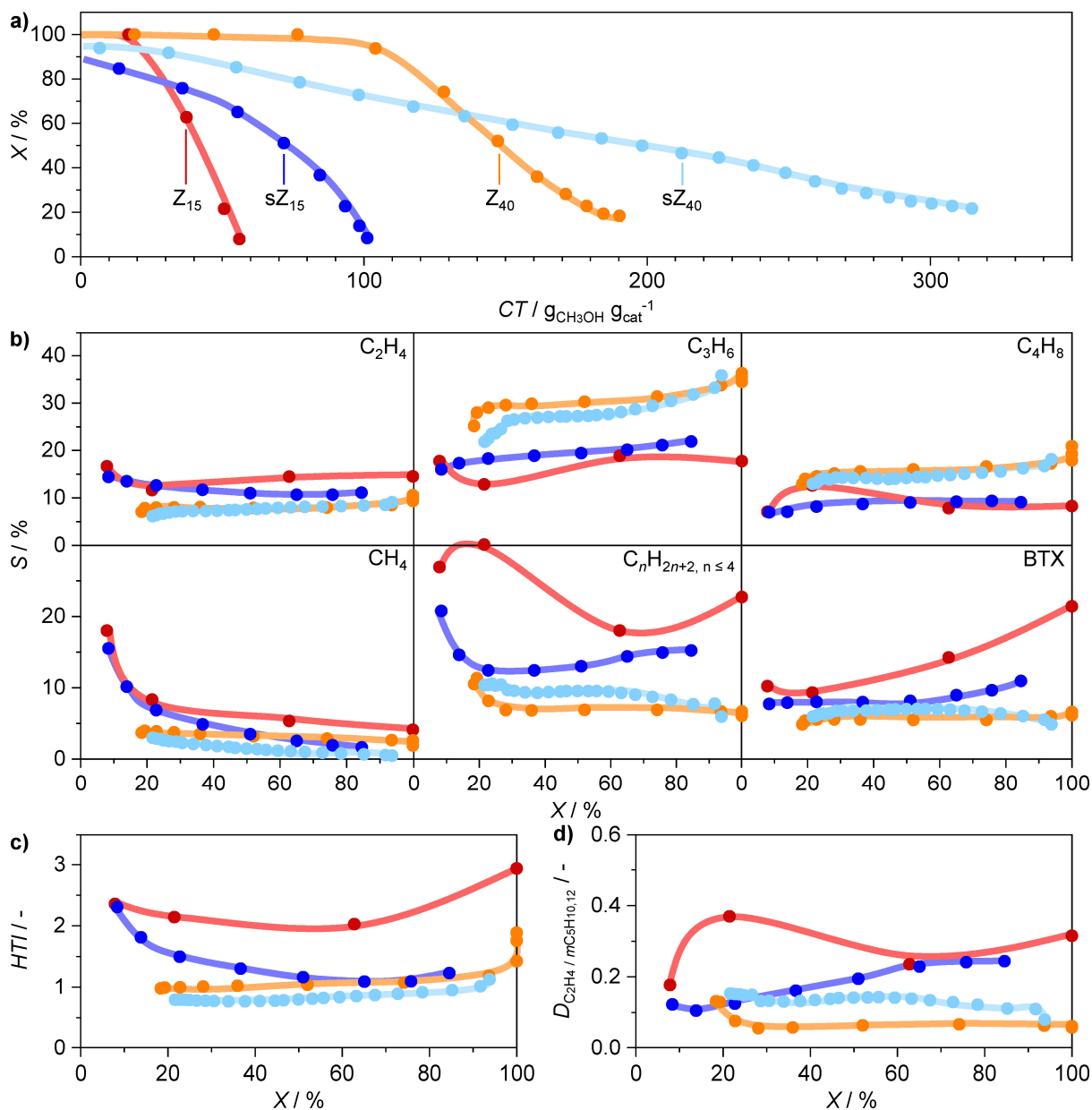


Fig. S6. a) Conversion versus cumulative turnover, b) selectivities to specific hydrocarbon products, c) hydrogen transfer index, and d) ethene:(2-methylbutane + 2-methylbutene) ratios of the Z₁₅, Z₄₀, sZ₁₅, and sZ₄₀ catalysts in the MTH reaction tests performed in the laboratory fixed-bed reactor with GC-FID detection. The color code in a) applies to all plots. Other conditions: CH₃OH:Ar = 19:81 mol%, $WHSV = 76 \text{ g}_{CH_3OH} \text{ g}_{cat}^{-1} \text{ h}^{-1}$, $T = 773 \text{ K}$, and $P = 1.6 \text{ bar}$.

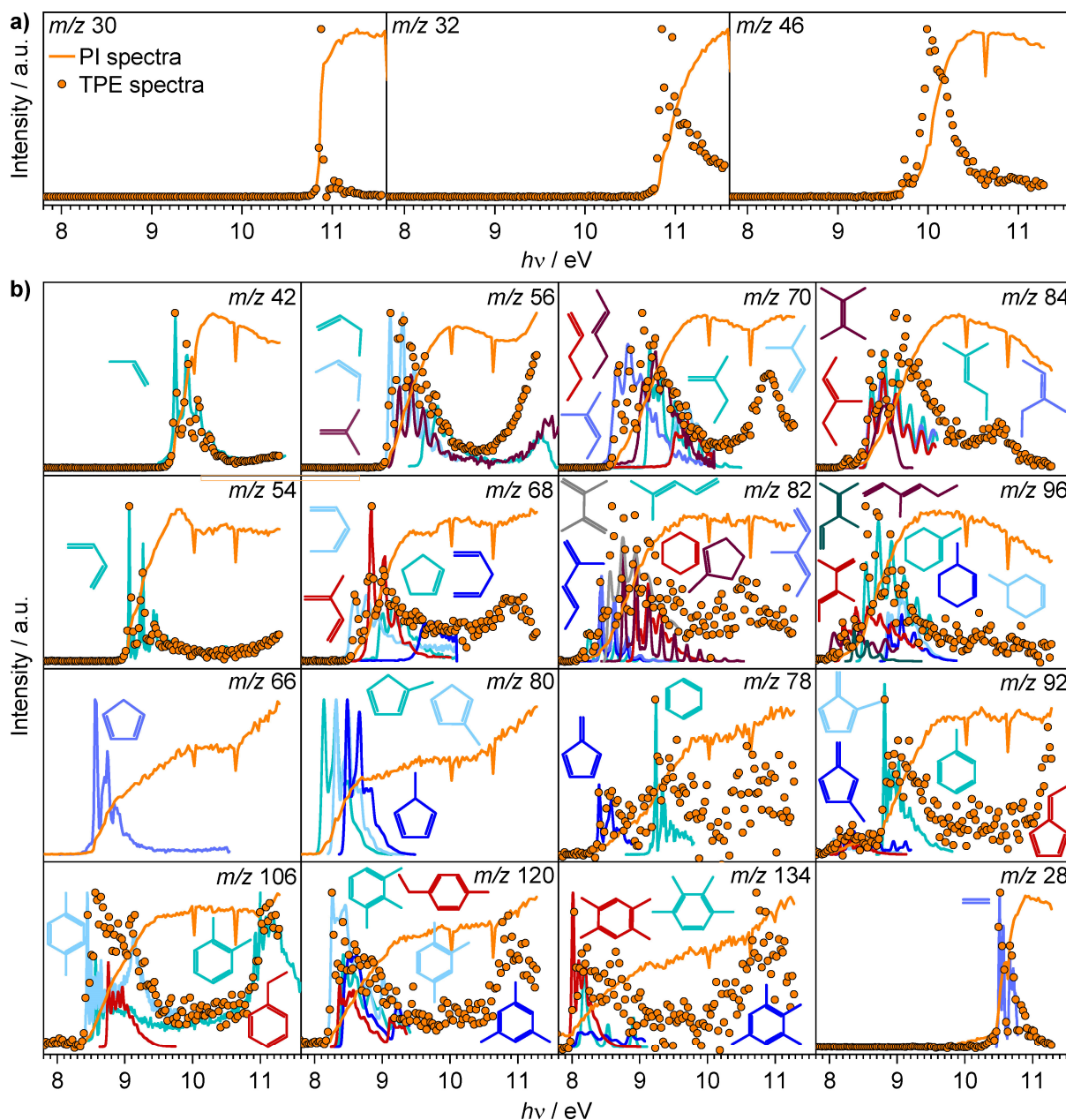


Fig. S7. Photoionization (PI) and photoion mass-selected TPE spectra of a) methanol, DME, and formaldehyde, and b) representative MTH products over Z_{40} . Frank–Condon simulation of TPE spectra of identified reaction species are presented along with respective spectra. Reaction conditions: $\text{CH}_3\text{OH}:\text{Xe}:\text{Ar} = 1.95:0.15:97.9$ mol%, $WHSV = 1.4 \text{ g}_{\text{CH}_3\text{OH}} \text{ g}_{\text{cat}}^{-1} \text{ h}^{-1}$, $T = 695 \text{ K}$, and $P = 0.4 \text{ bar}$.

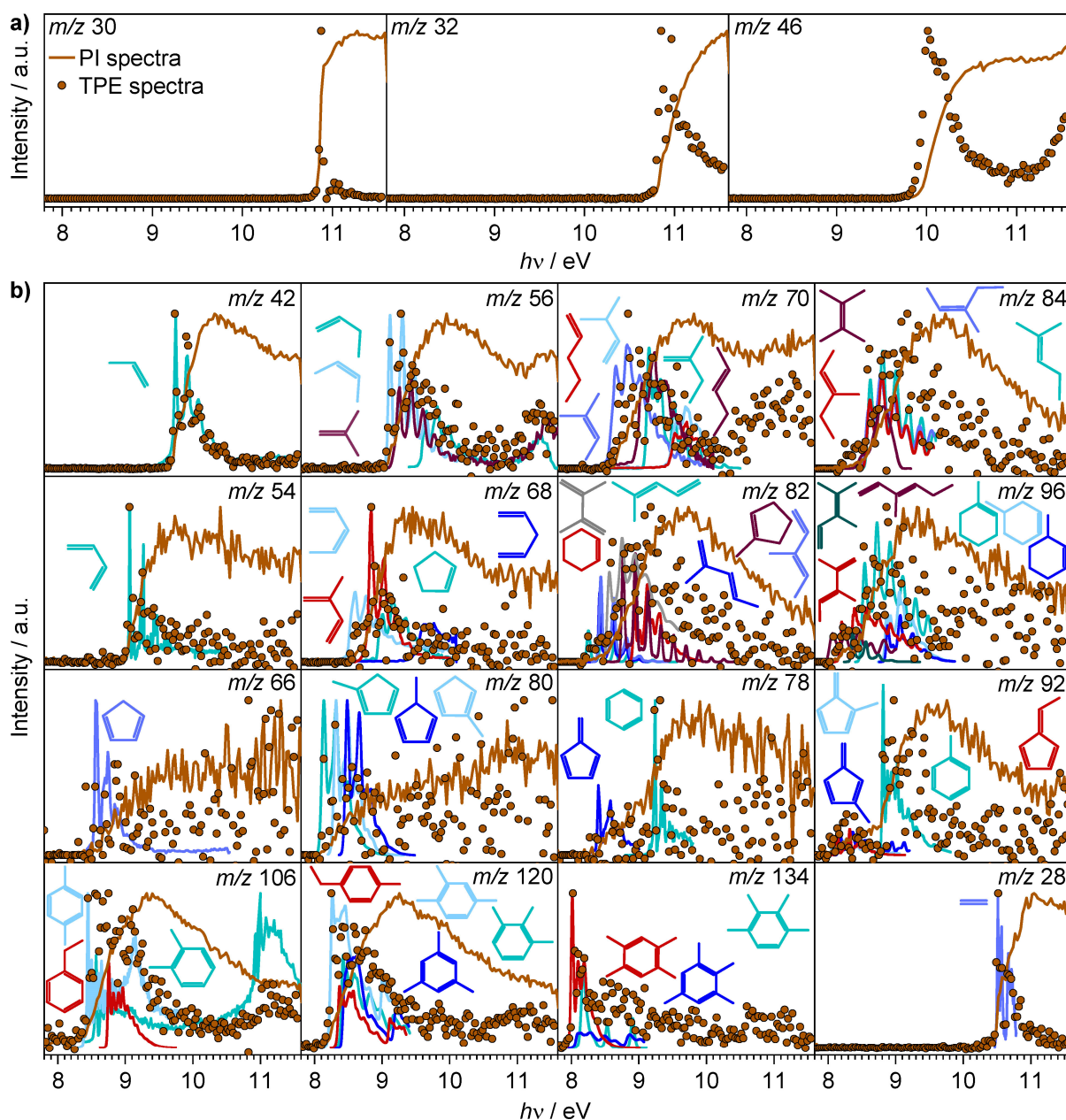


Fig. S8. Photoionization (PI) and photoion mass-selected TPE spectra of a) methanol, DME, and formaldehyde, and b) representative MTH products over Z_{40} in the presence of formaldehyde co-feed. Frank–Codon simulations of identified reaction species are presented along with the respective experimental spectra. Reaction conditions: $\text{CH}_3\text{OH}:\text{CH}_2\text{O}:\text{Xe}:\text{Ar} = 1.95:1.1:0.15:96.8$ mol%, $WHSV = 1.4 \text{ g}_{\text{CH}_3\text{OH}} \text{ g}_{\text{cat}}^{-1} \text{ h}^{-1}$, $T = 678 \text{ K}$, and $P = 0.4 \text{ bar}$.

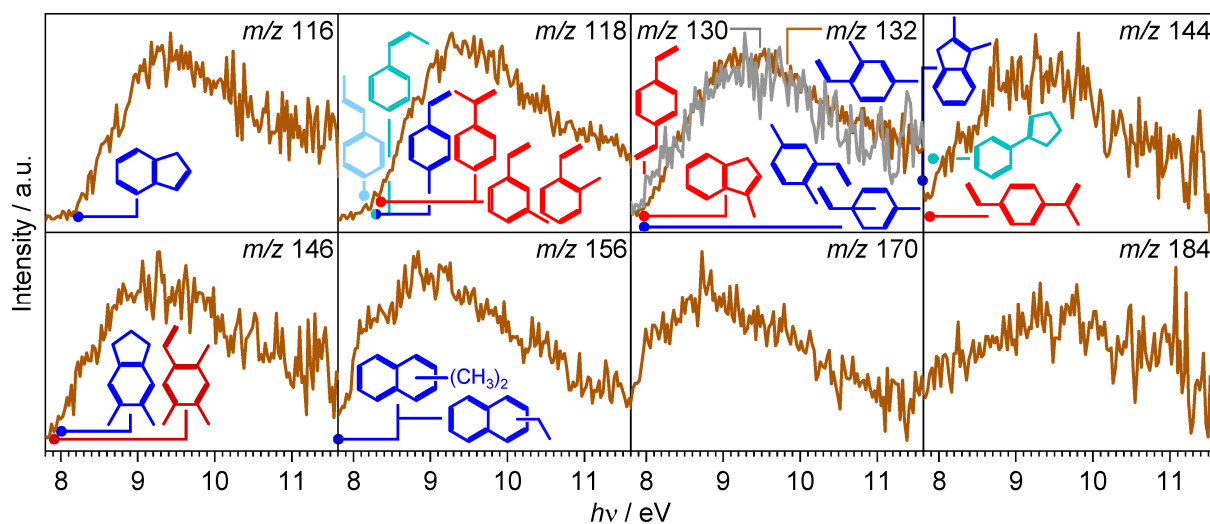


Fig. S9. Photoionization and photoion TPE spectra of the characteristic high molecular weight species detected during the MTH reaction over Z_{40} in the presence of formaldehyde co-feed. G4-computed ionization energies of the potential spectral carriers are presented along with the respective spectra. Reaction conditions correspond to those specified in **Fig. S6**.

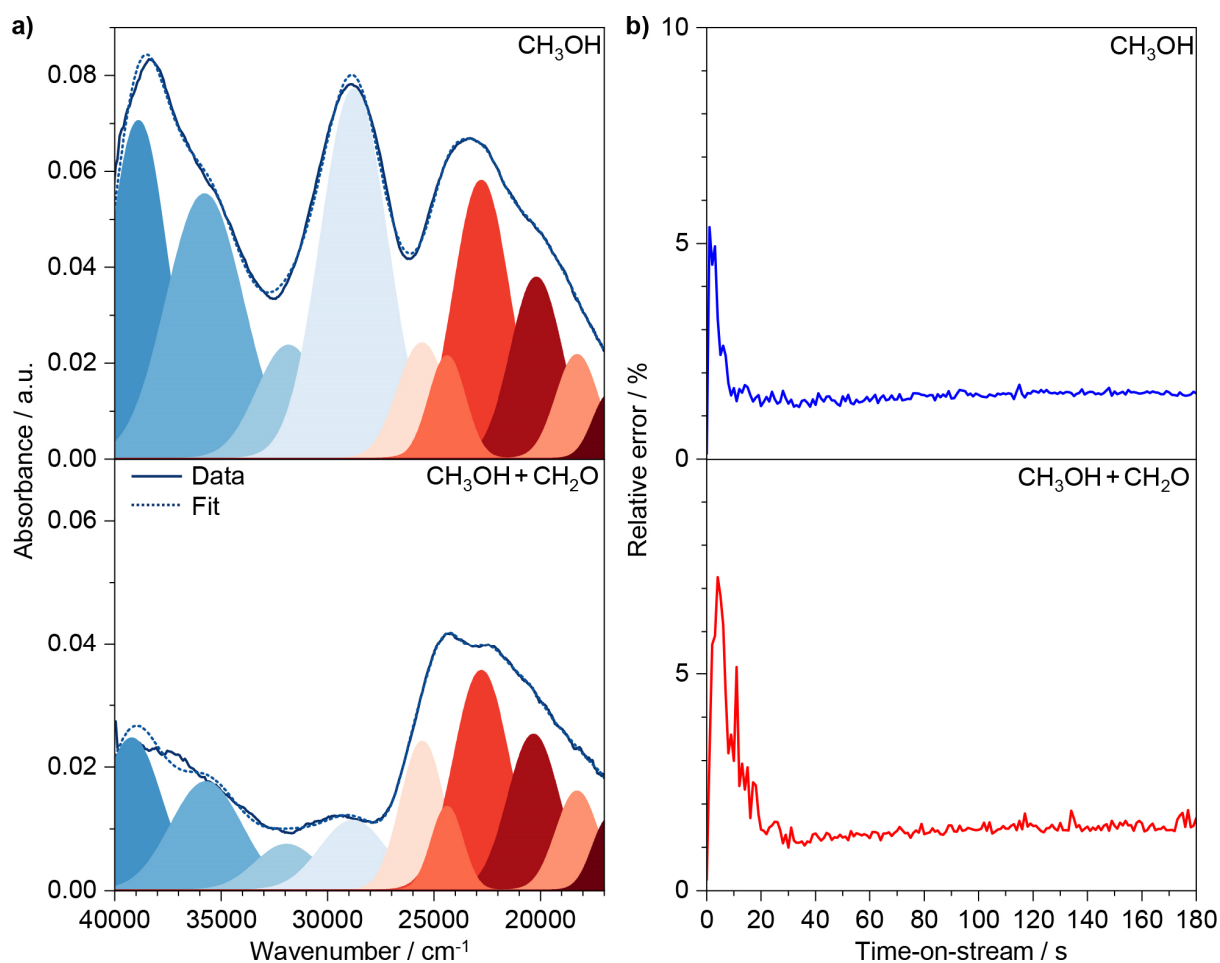


Fig. S10. a) Representative DR-UV/Vis spectra acquired during the MTH reaction over Z_{40} in the absence (top) and in the presence (bottom) of formaldehyde in the feed and their deconvolution into the Gaussian peaks. The assignment of the respective peaks is provided in **Table S3**. b) Relative error of the deconvolution procedure for spectra acquired at different time-on-stream. Reaction conditions: $\text{CH}_3\text{OH}:\text{CH}_2\text{O}:\text{Ar} = 10.6:0(0.2):89.4(89.2)$ mol%, $WHSV = 41 \text{ g}_{\text{CH}_3\text{OH}} \text{ g}_{\text{cat}}^{-1} \text{ h}^{-1}$, $T = 673 \text{ K}$, and $P = 1.2 \text{ bar}$.

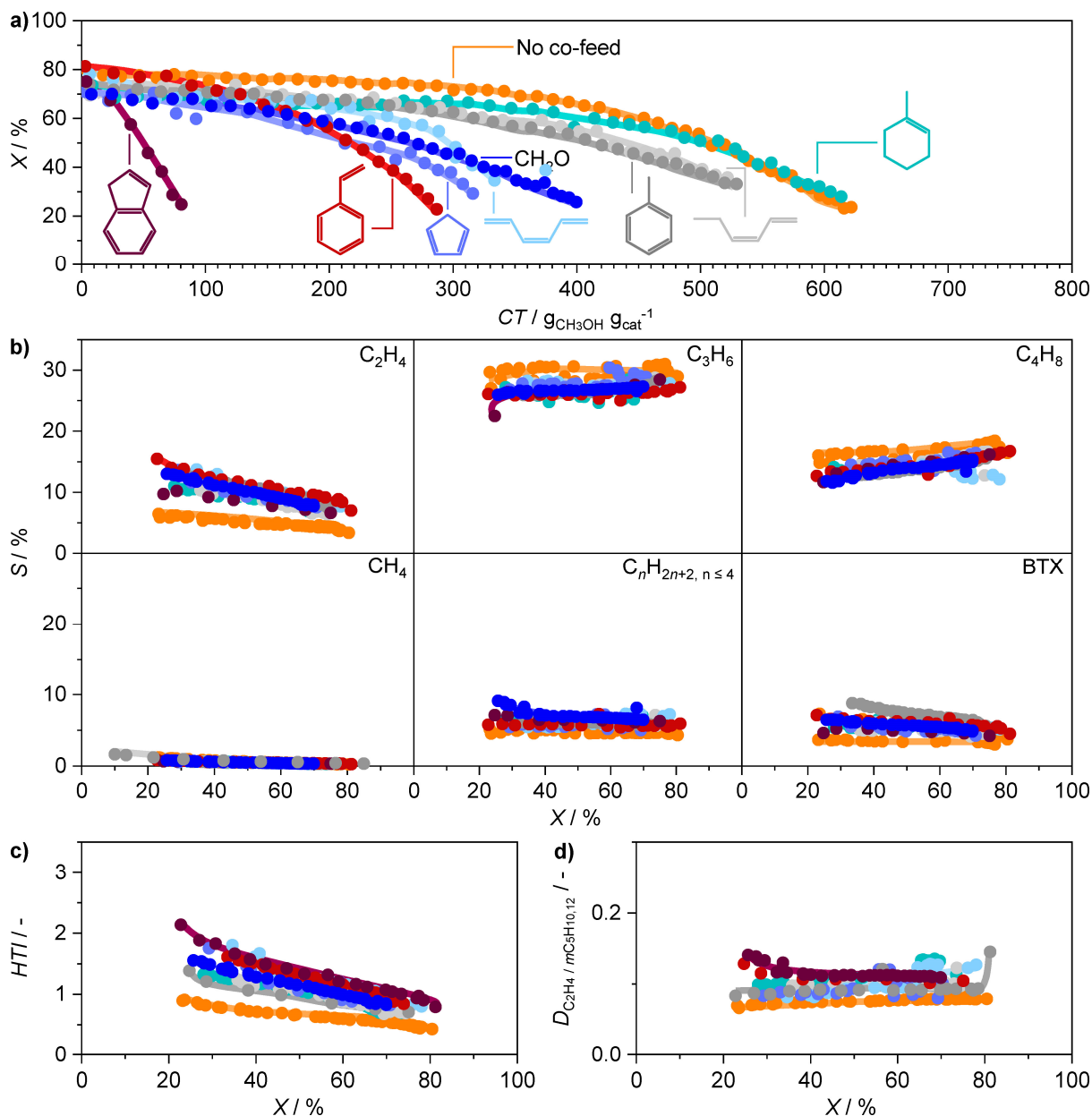


Fig. S11. a) Conversion versus cumulative turnover, b) selectivities to specific hydrocarbon products, c) hydrogen transfer index, and d) ethene:(2-methylbutane + 2-methylbutene) ratios of the Z₄₀ catalysts in the absence and in the presence of different co-feeds in the MTH tests performed in the laboratory fixed-bed reactor with GC-FID detection. The color code in a) applies to all plots. Reaction conditions: CH₃OH:co-feed:Ar = 21:0.4(0):88.6(89) mol% , $WHSV = 76 \text{ g}_{CH_3OH} \text{ g}_{cat}^{-1} \text{ h}^{-1}$, $T = 673 \text{ K}$, and $P = 1.6 \text{ bar}$. The addition of small amounts of formaldehyde significantly increases the selectivity to ethene and BTX, as well as the HTI and $D_{C_2H_4} / mC_5H_{10,12}$ parameters and catalyst propensity to coking. This corroborates the

propagation of the arene cycle and the coke-forming reaction sequences by formaldehyde. Similarly, when proposed formaldehyde-mediated reaction intermediates (refer to **Scheme S1** of the main text), are co-fed, they induce comparable changes in product selectivities, *HTI* and $D_{C_2H_4} / m_{C_5H_{10,12}}$ as formaldehyde. However, the model co-feeds exhibit more notable variations in terms of their impact on *CT* capacity, which decreased in the following order: methylcyclohexene < toluene \approx hexadiene < formaldehyde < cyclopentadiene \approx hexatriene < vinylbenzene \ll indene. The higher deactivating potential of hexatriene and its cyclic analog cyclopentadiene compared to hexadiene and its cyclic analog methylcyclohexene indicates that the deactivating potential of formaldehyde likely stems from its ability to facilitate the transformation of dienes into more conjugated triene (polyene) molecules via Prins condensation, bypassing hydrogen-transfer reactions. Additionally, the substantial reduction in *CT* observed in the presence of vinylbenzene, and particularly indene, is consistent with the hypothesis that the formation of these compounds during the later stages of formaldehyde-mediated reactions can significantly diminish the lifespan of the catalyst.

S4. Supplementary references

- 1 L. Milaković, P. H. Hintermeier, Y. Liu, E. Baráth and J. A. Lercher, *Angew. Chem. Int. Ed.*, 2021, **60**, 24806–24810.
- 2 S. Ilias, R. Khare, A. Malek and A. Bhan, *J. Catal.*, 2013, **303**, 135–140.
- 3 Z. Pan, A. Bodi, J. A. Van Bokhoven and P. Hemberger, *Phys. Chem. Chem. Phys.*, 2022, **24**, 3655–3663.
- 4 L. Kilburn, M. DeLuca, A. J. Hoffman, S. Patel and D. Hibbitts, *J. Catal.*, 2021, **400**, 124–139.
- 5 I. Andrew and R. J. Gorte, *J. Catal.*, 1984, **89**, 150–158.
- 6 S. G. Lias, J. E. Bartmess, J. F. Liebman, J. L. Holmes, R. Levin and W. G. Mallard, in *NIST Chemistry WebBook, NIST Standard Reference Database Number 69*, eds. P. J. Linstrom and W. G. Mallard, National Institute of Standards and Technology, 2023.
- 7 T. A. Cool, J. Wang, K. Nakajima, C. A. Taatjes and A. McIlroy, *Int. J. Mass Spectrom.*, 2005, **247**, 18–27.
- 8 G. Cooper, J. E. Anderson and C. E. Brion, *Chem. Phys.*, 1996, **209**, 61–77.
- 9 Y. Li, J. Yang and Z. Cheng, Center for NSRL Photoionization Mass Spectrometry, <http://flame.nsrllustc.edu.cn/database/data.php>.
- 10 J. Wang, B. Yang, T. A. Cool, N. Hansen and T. Kasper, *Int. J. Mass Spectrom.*, 2008, **269**, 210–220.
- 11 F. Z. Chen and C. Y. R. Wu, *J. Phys. B At. Mol. Opt. Phys.*, 1999, **32**, 3283–3293.
- 12 T. A. Cool, K. Nakajima, T. A. Mostefaoui, F. Qi, A. McIlroy, P. R. Westmoreland, M. E. Law, L. Poisson, D. S. Peterka and M. Ahmed, *J. Chem. Phys.*, 2003, **119**, 8356–8365.
- 13 H. Koizumi, *J. Chem. Phys.*, 1991, **95**, 5846–5852.
- 14 B. Yang, J. Wang, T. A. Cool, N. Hansen, S. Skeen and D. L. Osborn, *Int. J. Mass Spectrom.*, 2012, **309**, 118–128.

- 15 J. W. Au, G. Cooper and C. E. Brion, *Chem. Phys.*, 1993, **173**, 241–265.
- 16 Z. Zhou, L. Zhang, M. Xie, Z. Wang, D. Chen and F. Qi, *Rapid Commun. Mass Spectrom.*, 2010, **24**, 1335–1342.
- 17 Z. Zhou, M. Xie, Z. Wang and F. Qi, *Rapid Commun. Mass Spectrom.*, 2009, **23**, 3994–4002.
- 18 D. Mores, E. Stavitski, M. H. F. Kox, J. Kornatowski, U. Olsbye and B. M. Weckhuysen, *Chem. - A Eur. J.*, 2008, **14**, 11320–11327.
- 19 J. Goetze, F. Meirer, I. Yarulina, J. Gascon, F. Kapteijn, J. Ruiz-Martínez and B. M. Weckhuysen, *ACS Catal.*, 2017, **7**, 4033–4046.
- 20 D. Fu, O. Heijden, K. Stanciakova, J. E. Schmidt and B. M. Weckhuysen, *Angew. Chemie Int. Ed.*, 2020, **59**, 15502–15506.
- 21 L. Treppe, C. Demaret, D. Wisser, B. Harbuzaru, A. Méthivier, E. Guillon, D. V. Benedis, A. Gomez, T. De Bruin, M. Rivallan, L. Catita, A. Lesage and C. Chizallet, *J. Phys. Chem. C*, 2021, **125**, 2163–2181.
- 22 K. Barbera, F. Bonino, S. Bordiga, T. V. W. Janssens and P. Beato, *J. Catal.*, 2011, **280**, 196–205.
- 23 X. Meng, M. Zhang, C. Chen, C. Li, W. Xiong and M. Li, *Appl. Catal. A Gen.*, 2018, **558**, 122–130.
- 24 S. Bordiga, C. Lamberti, F. Bonino, A. Travert and F. Thibault-Starzyk, *Chem. Soc. Rev.*, 2015, **44**, 7262–7341.